

## **4.1 Introduction**

Over the past decades, carbon-based materials were widely studied and used in various technological fields because of unique properties of all carbon allotropes like fullerene, carbon nanotube and graphene [1-4]. Out of all carbon allotropes, graphene has enticed substantial research concern since its successful fabrication in 2004 [4]. The symmetrical hexagonal honeycomb structure of graphene leads us to its remarkable physical properties [5-10]. Thorough analysis of graphene proves it to be the promising material for nanoelectronics and spintronics [11-12]. The research of two dimensional (2D) materials which became popular with the discovery of graphene further lead the synthesis and prediction of monolayer of hexagonal boron nitride (h-BN), silicon, transition metal sulfides, phosphorous, arsenic, antimonite and many more [13-23]. Due to the unique and useful electronic, optical and mechanical properties of these 2D materials, evolution in nanodevices and nanoelectronics has been established [5-12]. 2D materials with conventional hexagonal structure have collected recognition due to the structural effect on properties of materials. This is because the formation of electronic structure in any material is typically associated with the position of atoms in the structure. Boron nitride (BN) nanostructures, which are analogous to carbon, are broadly studied due to their enormous chemical and thermal stability as a result of their exceptional properties [24-25]. The h-BN consists of large bandgap contrary to graphene which is the semimetal, acquire umpteen excellent properties analogous to graphene like strong mechanical properties, high thermal conductivity and thermal stability. This can be attributed to their geometrical similarity [26-27]. The carbon-carbon bonding in graphene is non-polar while boron-nitrogen bonding in h-BN is highly polar [28-29]. On account of these unique

properties, h-BN found its utilization in lubricants, dielectric materials, insulators in electronic devices, etc. [30-31].

The presence of another novel structures in 2D materials was determined by the existence of square-octagonal pair in monolayer of BN developed on Cu(111) surface [32] as defect mode of h-BN. This existence of these square-octagonal pair in h-BN was also reported by Liu et al. [33]. Consequently, similar structures of GaN [34] and ZnO [35] were predicted and studied. Nonetheless, to the best of our knowledge the feasibility of identical periodic structures with square-octagonal pairs of boron and nitrogen is yet to be explored despite of its experimental existence. Therefore, motivated through the work of Liu et al. [33] and prediction of GaN along with ZnO, we investigated haeckelite boron nitride (haeck-BN) using density functional theory.

During past decades, deoxyribonucleic acid (DNA) and ribonucleic acid (RNA) have received a great attention as they are the fundamental elements of genome and center of all biological systems. With purine as the base compound of DNA, the fundamental building blocks of nucleotides are nucleobases that contain all the information. Several studies are reported that specify the sensing mechanism of nucleobases with nanostructures [36-43]. For the essential DNA research, the major advantages of h-BN over graphene are their lower hydrophobicity and thickness as compared to spacing of nucleotides in single stranded DNA [44-45]. In comparison with graphene, because of the presence of different boron and nitrogen atoms in BN nanostructures, Zhi et al. [38] found the strong interactions between BN nanostructures and nucleobases. Transition metal chalcogenides like MoS<sub>2</sub> have also been reported for the sensing of nucleobases by altering its surface with gold [46]. These entire

studies have improved our understanding about the use of boron nitride nanostructures (BNNs) in bio-applications [43, 47-49].

Inspired by achievement of BNNs in sensing and detecting biomolecules, we analyzed the newly predicted haeck-BNNs as potential biosensor. The haeckelite structure of BNNs is expected to interact otherwise with the adsorbate (akin to porous materials) due to their distinct distance and bond angles as a result of octagonal and square ring structure. Moreover, 2D haeckelite structure of BN has not been investigated for bio-sensing applications. Present work focuses on the structural, electronic and vibrational properties of haeck-BN. The possibilities of h-BN to be used in electronic devices are realized through electronic properties, while phonon properties present its use in understanding its thermal properties besides confirming the dynamical stability [50-56]. Subsequently we investigate the interaction mechanism of five nucleobases, namely, adenine (A), thymine (T), guanine (G), cytosine (C) and uracil (U) over haeck-BN. Ab-initio calculations were carried out to reveal dispersion effect on the interaction of considered systems. Accordingly, in present study, we uncover the nature of adsorption of all five nucleobases with haeck-BN to acquire an atomic scale perspective for numerous applications [57-58].

## **4.2 Computational Methods**

All calculations in the present study were performed using density functional theory (DFT) based on first principles calculations with a plane wave pseudopotential method as implemented in Quantum Espresso code [59]. The ground state parameters of all the structures were relaxed under Broyden–Fletcher–Goldfarb–Shanno algorithm (BFGS) [60]. The

Generalized gradient approximation (GGA) was used for exchange correlation functional in which the energy was parameterized by Perdew–Burke–Ernzerhof (PBE) [61]. The energy cut-off values for charge density and plane wave basis set were 80 Ry and 800 Ry respectively, were used for single particle functions, which were sufficient to fully converge the lattice parameters and total energy. In reciprocal lattice space integral calculations, we used 16 X 16 X 1 k-point grids for the unit cell and 8 X 4 X 1 for the (2 X 3) supercell in the Monkhorst-pack scheme [62]. The calculations of vibrational properties were performed by employing the density functional perturbation theory (DFPT) implemented in Quantum Espresso code [63]. Dynamical matrix for 2D monolayer of haeck-BN was calculated using 10 X 10 X 1 q mesh and by applying acoustic sum for  $q \rightarrow 0$ . The phonon frequencies calculation along the entire Brillouin Zone (BZ) is an assurance of dynamical stability, which was calculated by the perturbation method in Quantum espresso package [63]. To understand the interaction of haeck-BN with five nucleobases, a comparative analysis was performed by structural optimization, adsorption energy calculation and density of states (DOS). The dispersion forces have been highlighted in the literature by a precise quantum mechanical description which explains the interaction of a molecule with a nanosurface [64]. Therefore, the Grimme’s dispersion correction [65] has been considered for the long range van der Waals interaction (*i.e.* 3 Å) between the nucleobases and haeck-BN monolayer. The adsorption energy  $E_{ad}$  has been calculated according to the following equation:

$$E_{ad} = E_{haeck-BN+nucleobase} - (E_{haeck-BN} + E_{nucleobase}) \quad (4.1)$$

where  $E_{(haeck-BN+nucleobase)}$ ,  $E_{(haeck-BN)}$  and  $E_{(nucleobase)}$  is the total energy of haeck-BN adsorbed by nucleobase (adenine (A), thymine (T), guanine (G), cytosine (C) and uracil (U)), energy of the

adsorbent haeck-BN monolayer, and is the total energy of the nucleobase (A, T, G, C and U) respectively.

### 4.3 Results and Discussion

#### 4.3.1 Structural and Electronic Properties

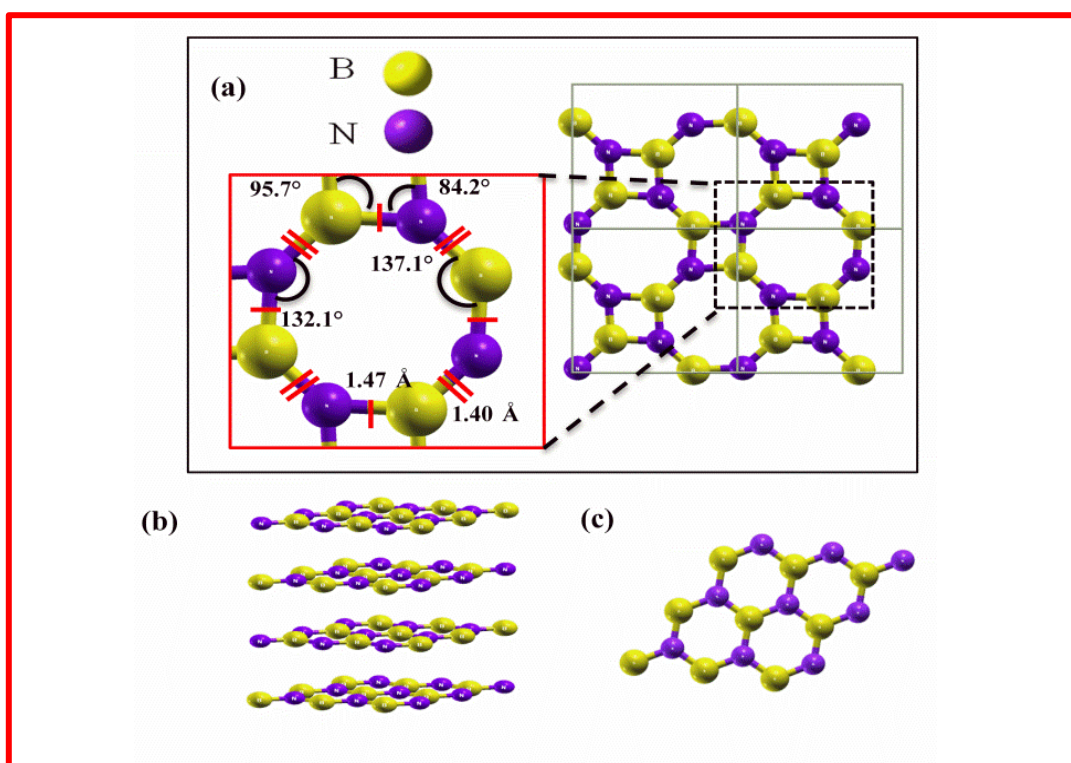


**Figure 4.1:** (a) Optimized structure of haeck-BN monolayer in addition with the enlarge view having bond length and bond angle, (b-c) Structure of bulk h-BN and 2D h-BN. Yellow and purple ball represents boron and nitrogen respectively.

To calculate and understand the structural and electronic properties of haeck-BN, we first optimized the geometry and related parameters of the primitive unit cell of the haeck-BN monolayer by calculating its lattice constants and ground state energy. The optimized structure of the haeck-BN monolayer is shown in Fig. 4.1(a). Figure 4.1(a) depicts the tetragonal primitive cell, with space group P4/mbm (127) for haeck-BN which is different from the bulk

and 2D h-BN (Fig. 4.1(b and c)). While bulk BN possesses P63/mmc (194), P63mc (186) and F-43m (216) space groups for bulk h-BN, wurtzite BN and zinc blende BN [66-67] respectively, the 2D h-BN consists hexagonal honeycomb lattice with P-62m (189) space group. The unit cell of the haeck-BN shows an atom situated at the center but not at the corner. The octagonal and square rings of haeck-BN give different interatomic distances and bond angles. The B–N has a bond distance of 1.402 Å and 1.475 Å in square and octagonal ring respectively. The square ring has 84.211° and 95.781° bond angles whereas in the octagonal ring, the bond angles are 132.10° and 137.11° respectively.

**Table 4.1:** Calculated Lattice ‘a’ (Å), Bond length (Å), Bond angle (°), Energy band gap  $E_g$  (eV), Fermi level energies  $E_F$ (eV) of haeck-BN.

System	Lattice a (Å)	Bond angle (°)	Bond length (Å)	$E_F$ (eV)	$E_g$ (eV)
BN-Haeckelite	4.929	84.21 and 95.78 (for square ring)	1.402 (bond in square ring)	-2.332	3.91
		132.10 and 137.11 (for octagonal ring)	1.475 (bond in octagonal ring)		

The bond length of B-N in haeck-BN is significantly different in comparison with bulk BN and 2D h-BN. In case of bulk BN and 2D h-BN, it varies from 1.45 to 1.56 Å [66]. The bond length of B–N in haeck-BN is 0.045 Å lesser in square ring, whereas it is larger by 0.025 Å in octagonal ring. This indicates the large structural difference in monolayers of h-BN and haeck-BN. The optimized lattice parameters as well as calculated bond length and bond angles are summarized in Table 4.1. The electronic band structure plays a key role to understand the

electronic properties of any material. The band dispersion carries important information about the mass of electron. Therefore, we have calculated the band structure of haeck-BN.

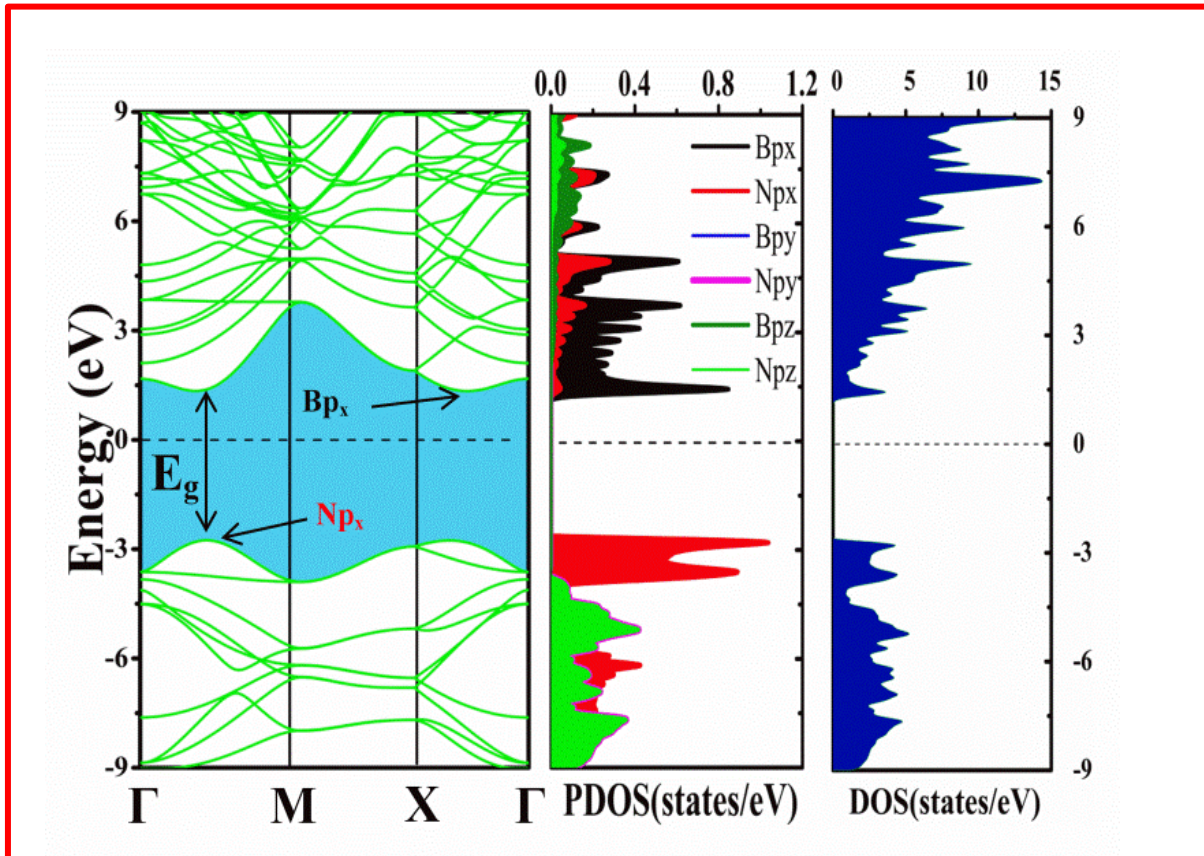


*Figure 4.2: Calculated band dispersion curve of haeck-BN. Along with total DOS and PDOS of haeck-BN at the right panel.*

The band structure of haeck-BN is calculated along the high symmetry directions of Brillouin zone (BZ) along  $\Gamma$ -M-X- $\Gamma$  of the BZ and is shown in Fig. 4.2. The highly dispersive nature of conduction bands indicate the small effective mass of electron. The calculated band dispersion of haeck-BN shows direct band gap of 3.9 eV between  $\Gamma$ -M directions of BZ. The band gap of 3.9 eV in the case of haeck-BN is lesser than the h-BN, z-BN and w-BN, which have large indirect band gap of 4.47 eV, 5.72 eV and 4.50 eV

respectively [66]. The haeck-BN is useful in optoelectronic and bio-sensing due to its lower direct band gap [68]. Boron and nitrogen atoms contribute equally in the electronic band structure of haeck-BN.

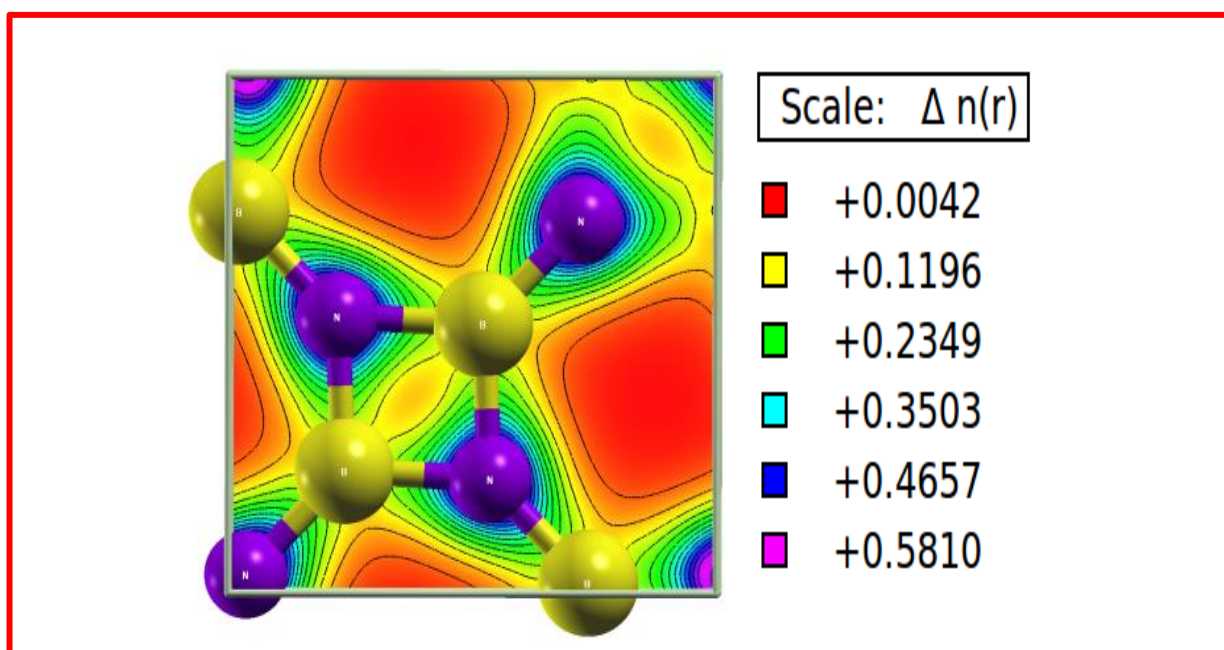


**Figure 4.3** Total charge density plot of haeck-BN. The blue colour represents the large value of electron charge density while red colour shows relatively low charge density

For further analysis of electronic contribution, we calculated the total and partial density of states of haeck-BN, which are shown in the right panel of Fig. 4.2. From the figure, we can see that the boron atoms contribute more in conduction band (between 2-6 eV) with its  $p_x$  orbitals, whereas,  $p_y$  and  $p_z$  show less contributions in the valence band (ranging from -4 to -8 eV). The contribution of nitrogen atom dominating in the valence band region with its  $p_x$  orbital electron between -2 to -4 eV, whereas, lower valence band region from -4 to -8 eV mainly formed by the  $p_y$  and  $p_z$  orbital electrons of nitrogen atoms. However, in bulk BN, the

B- $p_z$  orbitals contribute in conduction band while, the N- $p_z$  electrons contribute in the valence band maxima [66].

To understand the chemical bonding and the charge transfer in haeck-BN, we calculated the charge-density along (110) plane and presented in the Fig. 4.3. The charge density plot indicates the covalent bonding between B and N atoms. The electronegativity values for B and N atoms are +0.1196 and +0.4657, respectively. The density is evenly distributed, which reveals that there is no vacancy. The charge accumulation is larger near nitrogen atom (blue color; +0.4657), which depicts the localization of electrons around it.

### **4.3.2 Vibrational Properties**

In order to understand the dynamical stability of any material, phonon dispersion calculations are important as it provides an insight into the mechanical, acoustic, spectroscopic, thermodynamic and dynamical properties at finite temperatures [50-53]. The phonon dispersion curves (PDC) calculated by the diagonalization of dynamic matrix, is a real test of dynamical stability [51, 69-70]. The calculated phonon dispersion curves for haeck-BN along the major symmetry directions of the Brillouin zone (BZ) together with the corresponding phonon density of states (PHDOS) are shown in Fig. 4.4. The N number of atoms results into the 3N phonon branches, including three acoustic and 3N-3 optical modes [64]. The unit cell of haeck-BN consists eight atoms which gives 24 phonon branches, while in 2D h-BN, there are six phonon branches due to two atoms per unit cell [66, 71-72]. According to the polarization, the modes are labeled, the letters ‘L’, ‘T’ and ‘Z’ stand for longitudinal, transverse and out-of-plane vibrations, respectively. Letters ‘A’ and ‘O’ represent the acoustic

and optical modes, respectively. The longitudinal acoustic (LA) and transverse acoustic (TA) modes are linear as per their character around the  $\Gamma$  point, whereas the out of plane acoustic (ZA) mode shows quadratic nature with wave vector, which is a characteristic of 2D layered materials [23, 72-73]. The quadratic nature of the ZA mode arises due to  $D_{6h}$  point group symmetry, which can be attributed to the lowest-order amplitude, strain energy, induced by this vibration, together associated with the arching of this out-of-plane bending mode induced in the monolayer [74].

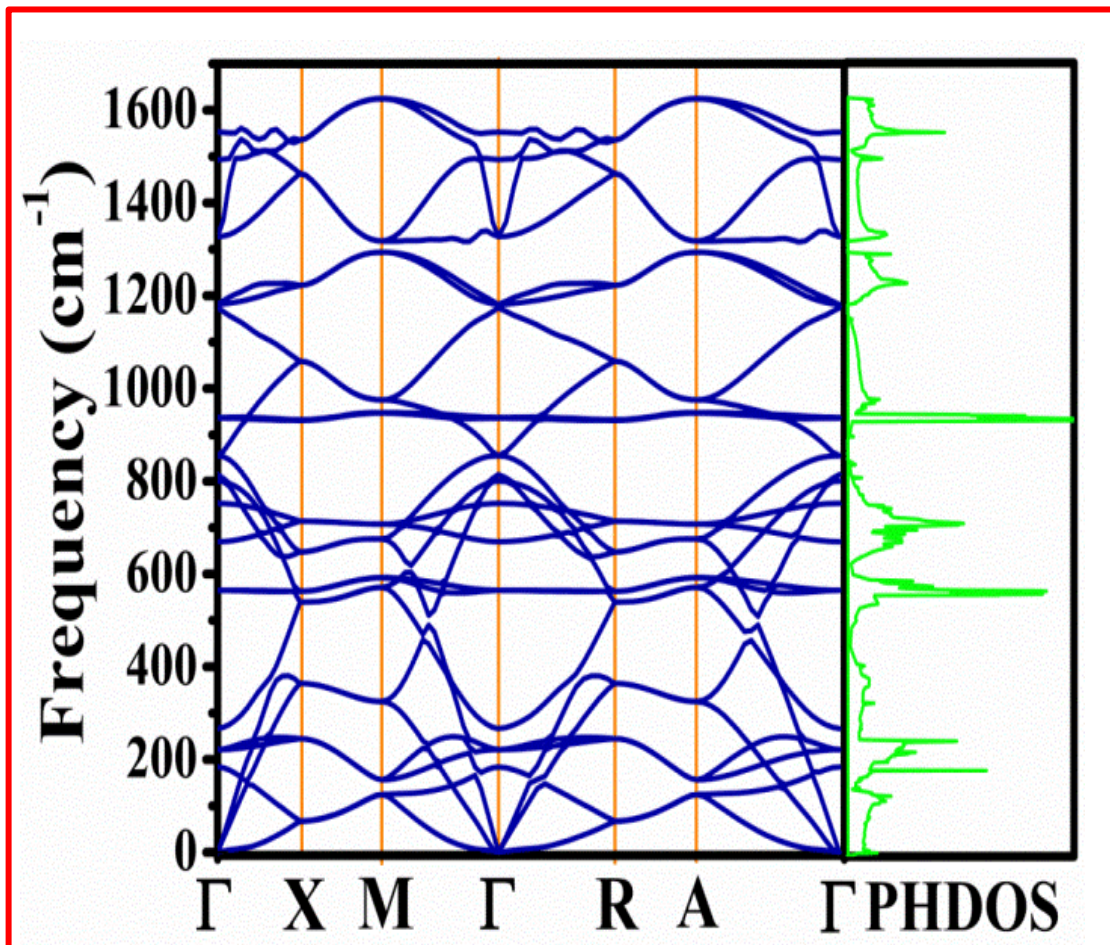


Figure 4.4: Phonon dispersion curve along with the phonon density of states (PHDOS).

There is no imaginary frequency in PDC confirming the dynamical stability of haeck-BN similar to other haeckelite compounds [34-35]. The quadratic ZA mode is closely associated with bending rigidity and lattice heat capacity of the nanosheet in the long-wavelength (small  $q$ ) region. Furthermore, there is a softening of the transverse acoustic (TA) and longitudinal acoustic (LA) modes which, indicates reduced group velocities. The reduced group velocities can be used to improve the thermoelectric figure of merit ZT as it reduces thermal conductivity [75]. The ZA mode, which behaves differently from TA and LA modes, will also have low group velocity due to a parabolic dispersion near the  $\Gamma$  point. There is no gap between acoustic and optical branches due to the negligible mass difference in boron and nitrogen atoms, similar to h-BN [72]. The phonons of the haeck-BN sheet show considerable softening as compared to the h-BN sheet, which can be attributed to the smaller elastic constants of haeck-BN than that of h-BN. There is nine singly (A) and six doubly (E) degenerated optical phonon modes, observed at the zone center as  $\Gamma = 9A + 6E$ . We observed that all 24 modes in haeck-BN are equally distributed throughout the frequency range varying from 0 to 1600  $\text{cm}^{-1}$ . The stability was further confirmed by calculating the PHDOS, as shown in the right panel of Fig. 4.4.

The PHDOS calculation is a real test of any phonon calculations as it requires calculation of phonon modes in entire BZ and helps to calculate lattice specific heat and other thermodynamic function [50-51]. The phonon density of states (PHDOS) is an essential dynamical property as it requires phonon frequencies in the entire Brillouin zone (BZ) and can be defined as [76]

$$g(\omega) = \frac{1}{N} \int_{BZ} \sum_j \delta[\omega - \omega_j(\vec{q})] d\vec{q} \quad (4.2)$$

where  $N$  represents the normalization constant that  $\int g(\omega)d\omega=1$ .  $g(\omega)d\omega$  is the ratio of the number of eigenstates in the frequency interval  $(\omega, \omega + d\omega)$  to the total number of eigenstates  $\omega_j(\bar{q})$  is the phonon frequency of the  $j^{\text{th}}$  phonon mode. The high frequency modes, which is due to the ionic bonding between  $sp^2$  hybridized B and N atoms in haeck-BN is quite similar to the previously reported  $sp^2$  hybrid boron nitride structures [72,77].

The dispersion of modes depends on the interaction strength; a mixing character of modes is observed due to the repulsion. The phonon modes along  $\Gamma$ -X directions come close and possess the same nature along X-M but show the splitting along M- $\Gamma$  directions of BZ. The flat band observed in the PDC causes the intense peaks at  $600$  and  $900\text{ cm}^{-1}$ . Additionally in the low frequency region, weak singularity is attributed to the strongly dispersed acoustical and lower optical phonon modes.

### **4.3.3 Adsorption Mechanisms**

To understand the adsorption mechanism between haeck-BN and five considered nucleobases, firstly we created the  $2 \times 3$  supercell of haeck-BN consisting of 48 atoms (24 B and 24 N atoms) to give large surface for interaction of nucleobases. We individually optimized the structural parameters of haeck-BN sheets followed by nucleobases adenine (A), thymine (T), guanine (G), cytosine (C) and uracil (U). The optimized structure of nucleobases A, T, G, C and U is presented in Figs. 4.5(a-e).

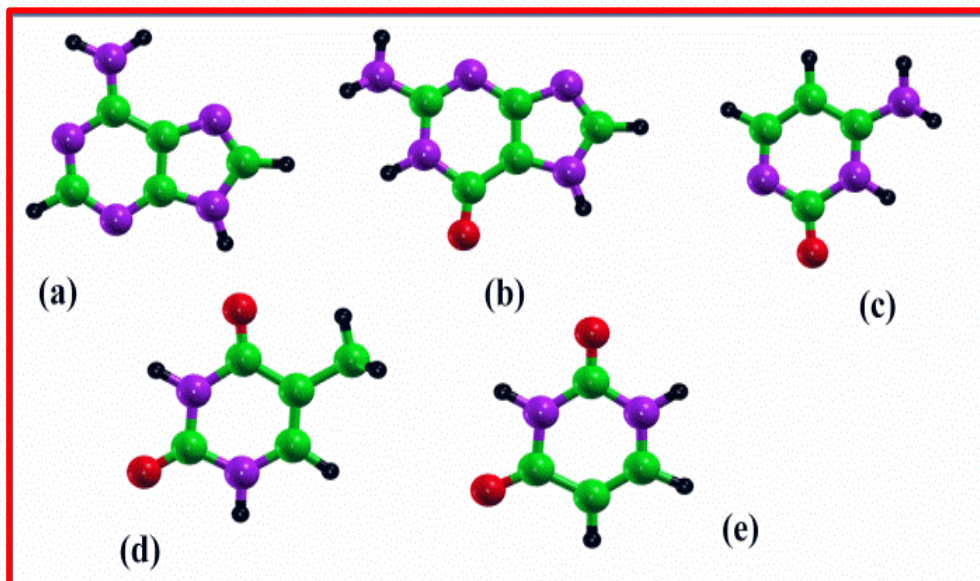


Figure 4.5 Optimized structures of five nucleobases A, G, C, T and U. Red, green, black and purple ball corresponds to oxygen, carbon, hydrogen and nitrogen atoms respectively

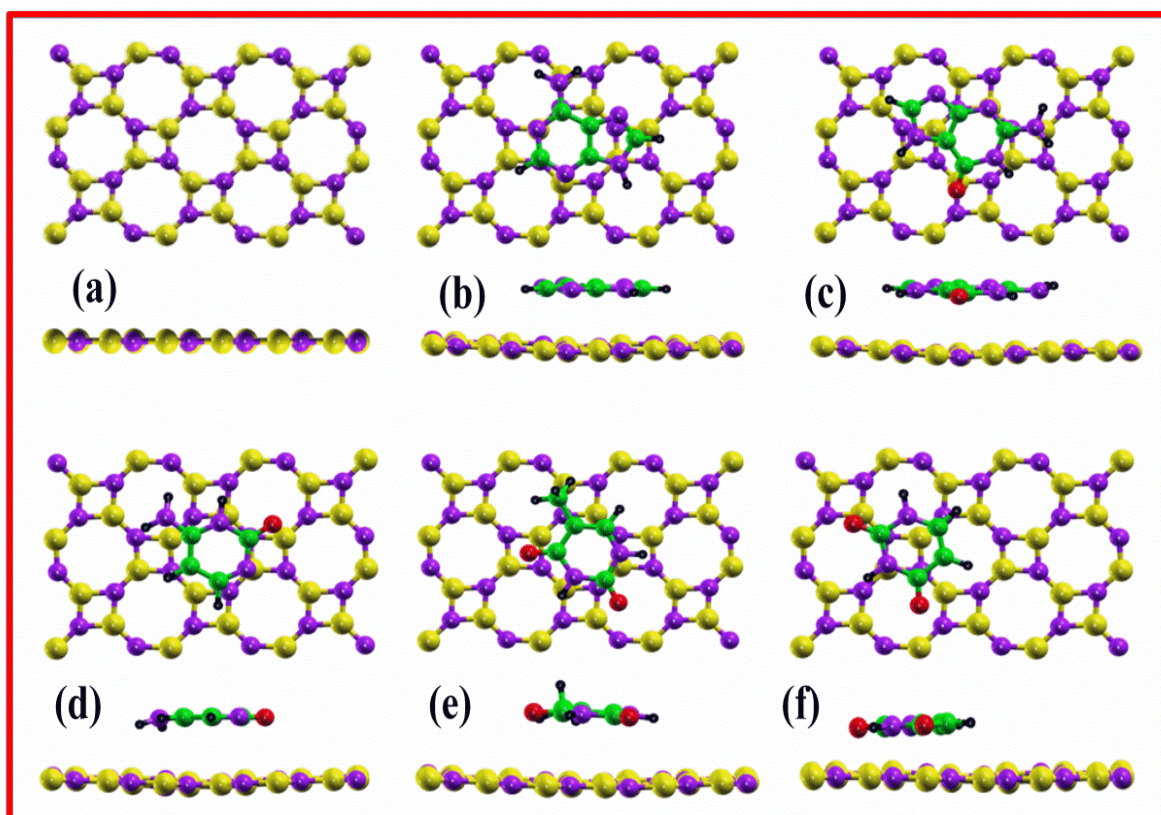
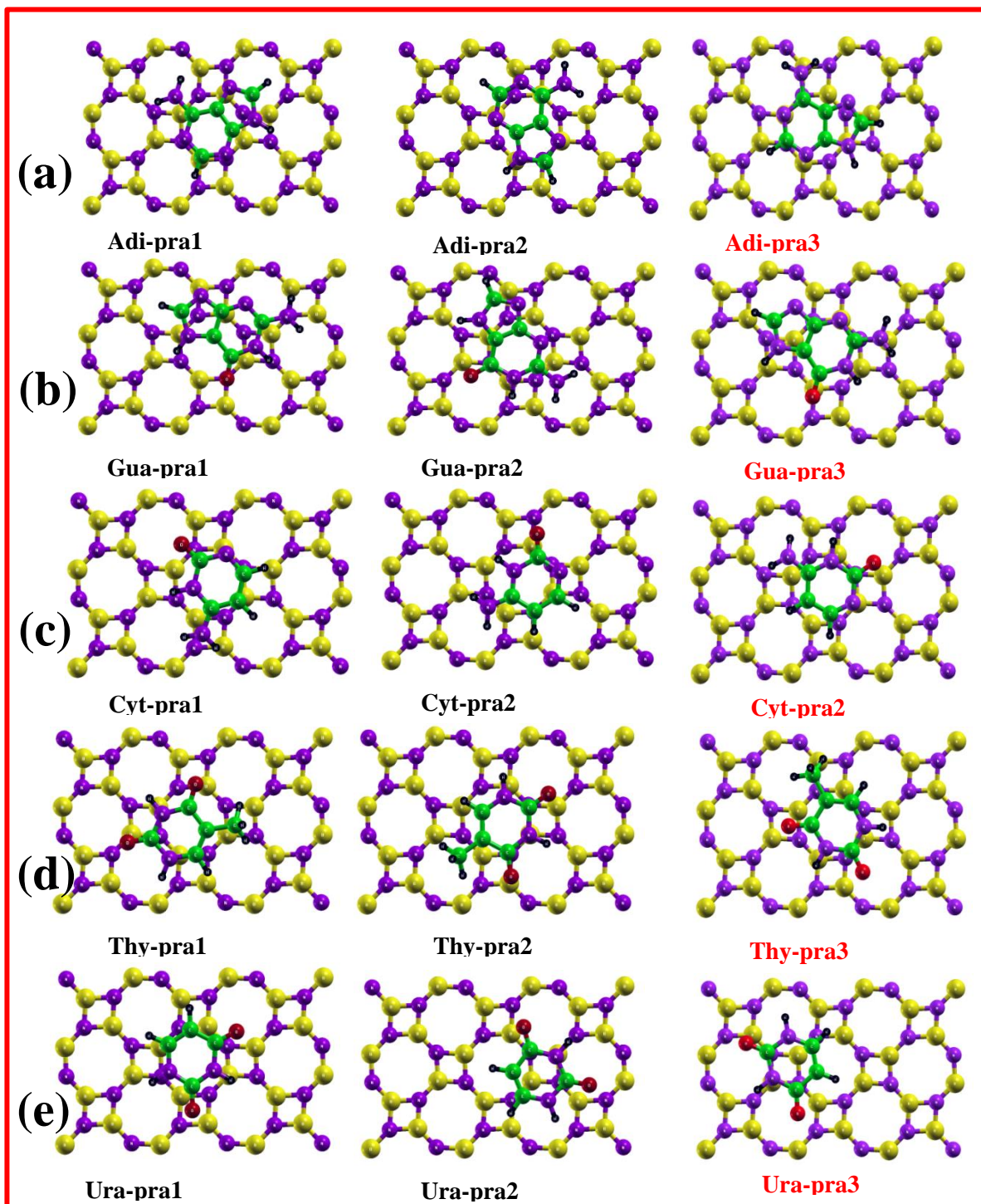


Figure 4.6 Optimized structures of (a) pristine haeck-BN and nucleobases adsorbed haeck-BN (b) Adenine (c) Guanine (d) Cytosine (e) Thymine (f) Uracil (top and side view).



**Figure 4.7:** Different parallel orientation of haeck-BN adsorbed by nucleobases (a) Adenine, (b) Cytosine, (c) Guanine, (d) Thymine, (e)Uracil.

Figs. 4.6 (a-f) present the optimized structures of pristine haeck-BN sheet along with

nucleobase-adsorbed haeck-BN sheet. We adopt parallel orientation for all adsorption study, as previous works proposed the parallel position of the nucleobases over BN nanostructures due to most stable structure [49, 78].

To obtain the ground state geometrical position, the calculation of structural optimization was primarily started by placing the molecule near the surface of haeck-BN, and followed by full structural relaxation. In the ground state configurations, the adsorbed molecules attained a distance in the range of 2.5–2.9 Å from haeck-BN. We can see that the chemical bonds are not formed due to the large distance between nucleobases and 2D haeck-BN which results in the physisorption of adsorbed nucleobases. Additionally, we carried out total energy calculations for every system by varying distances in the range of 1-4 Å from haeck-BN to confirm the nature of adsorption. We observed that when molecule is in the range between 2.5-2.9 Å, the energy is minimum that supports our full geometry optimization.

*Table 4.2: Calculated total energy of nucleobase adsorbed haeck-BN system. Red color represents minimum energy.*

System	Orientation			
	Perpendicular	Parallel		
		Parallel (1)	Parallel (2)	Parallel (3)
A	-805.67409951	-805.69333844	-805.70168216	<b>-805.70177593</b>
G	-839.36709371	-839.37120249	-839.39640827	<b>-839.39961217</b>
C	-787.02532204	-787.03926981	-787.04579516	<b>-787.04842003</b>
T	-813.63395282	-813.72114341	-813.72384597	<b>-813.72913714</b>
U	-799.35689170	-798.91355371	-798.85654916	<b>-799.37783694</b>

*Table 4.3: Calculated total energy of nucleobase adsorbed haeck-BN system with different orientation. Red color represents minimum energy.*

Distance (Å)	A	G	C	T	U
1.0	-797.14563569	-827.24450277	-778.32027206	-790.40151271	-793.01554085
1.5	-803.32734246	-835.14560366	-784.52685720	-801.55327009	-797.48784613
2.0	-805.07205702	-837.96243467	-786.28344130	-811.496918992	-798.86362140
2.5	-805.59573819	-839.04827443	-786.89557762	-813.26327259	-799.29076560
<b>Optimized</b>	<b>-805.70177593</b>	<b>-839.39961317</b>	<b>-787.04842003</b>	<b>-813.72913714</b>	<b>-799.37783694</b>
3.0	-805.69647630	-839.38631967	-787.03703933	-813.71807435	-799.39073438
3.5	-805.69071475	-839.38548052	-787.03216000	-813.71031933	-799.36672226
4.0	-805.67720738	-839.37047296	-787.02507247	-813.65860629	-799.35612839

We have also examined different orientations (Fig. 4.6) of nucleobases for better insight, and tabulated the total energies of these configurations together with distances and orientations in Tables 4.2 and 4.3. As the distance between nucleobases and haeck-BN sheet is large, i.e.,  $\sim 2.8$  Å, the nature of adsorption is physical (physisorption), (as can be seen in Table 4.4). The elimination of any possible covalent bond is confirmed from the large distance between nucleobases and haeck-BN. Dispersion correction was included in the present study to take long range van der Waals interaction in consideration as the adsorption energy is increased 8-10 times than the normal PBE calculation [43]. The new D3 [79] correction was not included in our study as both D2 and D3 corrections bring similar results on condition with non-covalent interactions [80]. The calculated adsorption energy ( $E_{ad}$ ) for A, G, C, T and U over haeck-BN are -0.662 eV, -0.742 eV, -0.660 eV, -0.668 eV and -0.525 eV, respectively,

with distances ( $d$ ) in the range of 2.7 Å to 2.9 Å. Our calculated adsorption energy gives better results than previously reported adsorption energies for h-BN and graphene [45, 81-83] which is due to the different structural and electronic properties of haeck-BN. The order of adsorption of all five nucleobases over haeck-BN is  $G > T > A \approx C > U$ , which is analogous to the adsorption order of these nucleobases with other BN and carbon nanostructures [45, 81-83].

**Table 4.4:** Adsorption energy  $E_{ad}$  (eV), vertical distance  $d$  (Å) of nucleobases from haeck-BN, bandgap  $E_g$  (eV) and Fermi energy  $E_F$  (eV).

System	haeck-BN	A	G	C	T	U
$E_g$ (eV)	3.913	3.109	3.199	2.869	3.309	3.340
$\Delta E_g$ (eV)	-	0.714	0.914	1.044	0.604	0.573
$E_{ad}$ (eV)	-	-0.662	-0.742	-0.660	-0.668	-0.525
$d$ (Å)	-	2.945	2.745	2.775	2.725	2.953
$E_F$	-4.199	-1.617	-0.424	-2.322	-2.344	-1.798
$\Phi$ (eV)	5.972	3.896	2.837	4.455	4.503	3.914

Comparable outcome of adsorption energies for five considered nucleobases on various nanomaterials is presented in Fig 4.8. This difference in the  $E_{ad}$  is due to the van der Waals force [84-85]. The highest adsorption energy is due to  $\pi$ - $\pi$  stacking as it decreases the repulsion because of overlapping of  $\pi$ -orbitals limiting the nucleobases to get repelled from the nanosurface. This results in superior  $E_{ad}$  on nanosurface [47-48].

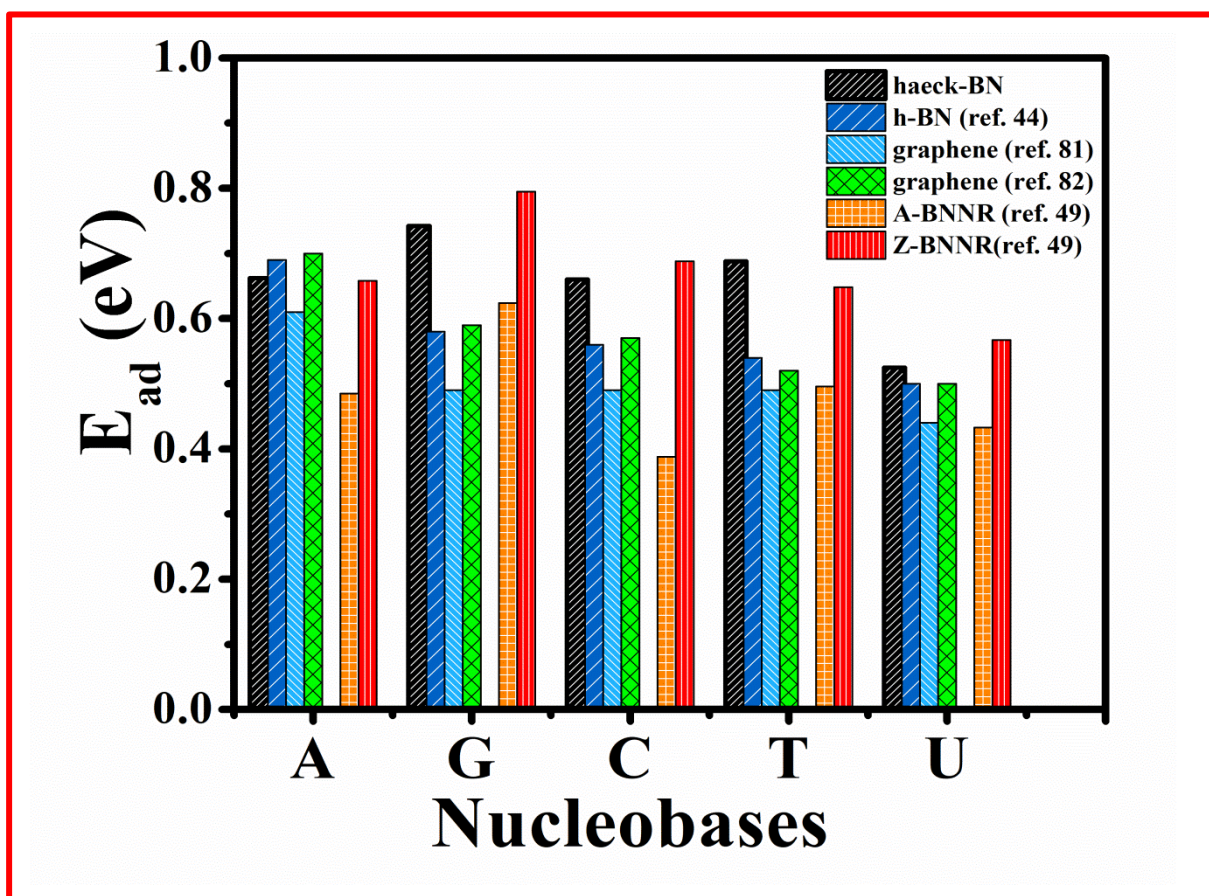
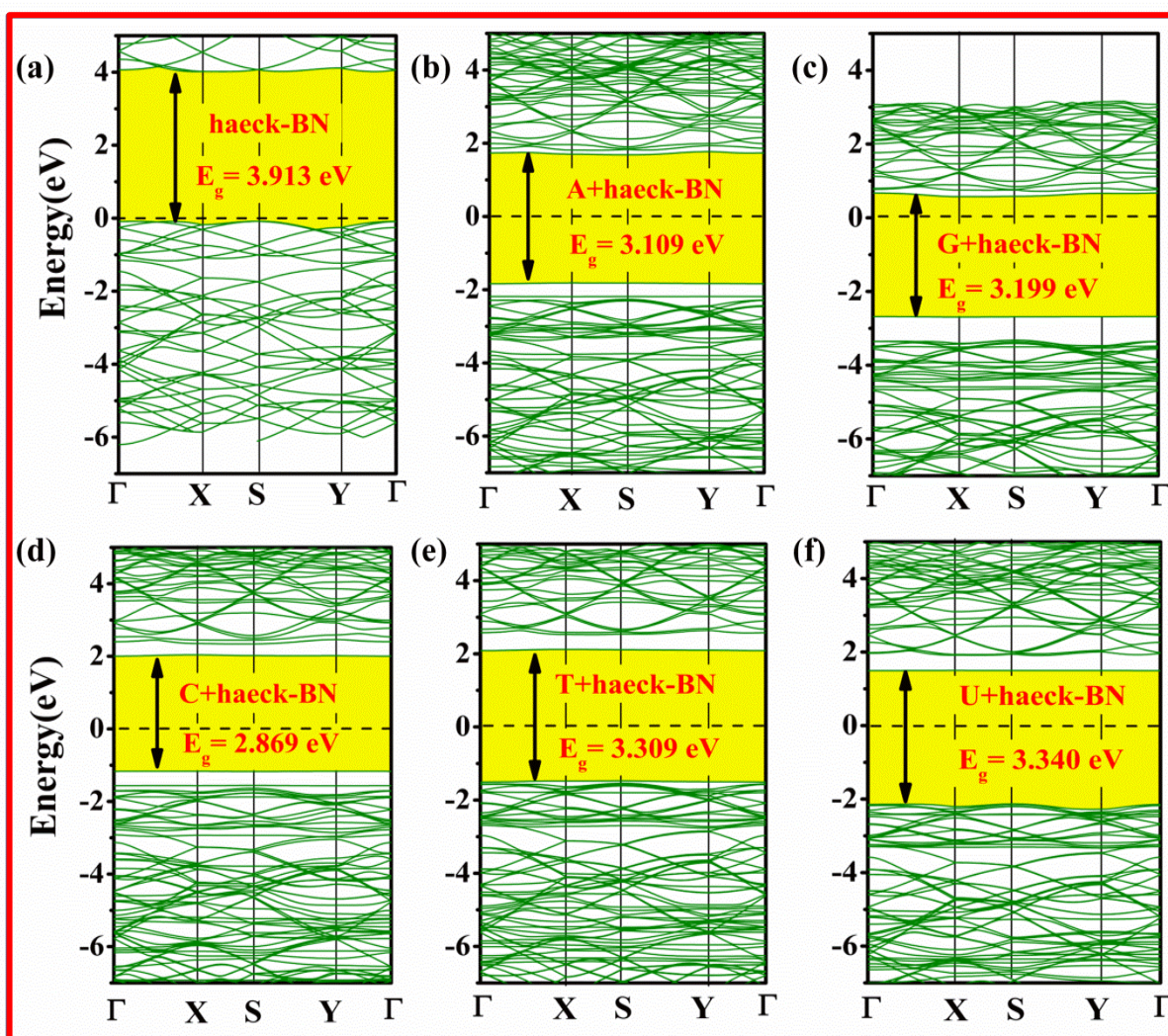


Figure 4.8: Comparative adsorption energies plot of nucleobases with different nanostructures.

The current study shows that the nucleobases are more adequately adsorbed on haeck-BN in comparison to graphene [82-83] and other BN nanostructures, like h-BN [45], BNNR [49] and BNNT [86]. The adsorption of nucleobases over haeck-BN sheet changes the electronic properties by analyzing the band structure, band gap, total and partial density of states (DOS and PDOS). Figure 4.9 shows the band dispersion curves of pristine and all five nucleobases adsorbed haeck-BN. An important modification in the band structure and band gap is seen in the band dispersion. After the adsorption of all five nucleobases, impure states are produced in the band structure which can be attributed to the p-orbital electrons of carbon, oxygen and nitrogen atoms and partial contribution of s-orbitals of hydrogen atom.



**Figure 4.9:** Band structure plots of haeck-BN (a) pristine and nucleobase adsorbed (b) Adenine (c) Guanine (d) Cytosine (e) Thymine (f) Uracil.

The presence of distinct flat bands in the conduction and valence band region in Fig. 4.9 is due to the quenching of kinetic energy of electrons [87]. Fig. 4.9(b) presents the band structure plot of adenine on haeck-BN which depicts the generation of impure states (flat bands) at the top of valence band. The flat bands generated in adenine molecule are due to the presence of  $p_x$  orbital electrons of nitrogen and carbon atoms. From the figure we can see that the flat bands are observed in the valence band at -1.9eV and -4 eV (attributed to  $p_x$  orbital of

nitrogen), while in conduction band it is near 2eV (attributed to  $p_x$  orbital of carbon). Likewise nature of bands in band structure is noticed for other nucleobases. In all considered nucleobases apart from adenine, oxygen atom contributes in formation of flat bands. Oxygen  $p_x$  orbital plays a significant role in valence bands in guanine (Fig. 4.9(c)) which is near -3 eV. Moreover, after adsorption of cytosine over haeck-BN (Fig. 4.9(d)), a large change in the band gap is found.

Several flat bands appear in both valence and conduction bands after thymine adsorption. However, uracil nucleobase generates less number of flat bands only in conduction band, which is due to its small size and number of atoms available for participation in construction of additional electronic states (Figs. 4.9 (e and f)). The reduction of band gap of haeck-BN (3.913 eV) was observed with the values 3.199 eV, 2.999 eV, 2.869 eV, 3.309 eV and 3.340 eV after nucleobases adsorption A, G, C, T and U, respectively.

We further investigated the Lowdin charge transport. The considerable charge transfer between all five nucleobases and haeck-BN shows that the interaction results in structural and electronic properties with the values 0.14e, 0.15e, 0.10e, 0.11e and 0.09e for A, G, C, T and U, respectively. Further we studied the charge transfer through charge density presented and HOMO-LUMO calculations. The charge density plots are presented in Fig 4.10. From the figure we can easily predict chemical bonding and also the nature of charge transfer between haeck-BN and considered nucleobases. The ability to donate or accept electrons of any material is represented by the Highest Occupied Molecular Orbital (HOMO) and the Lowest Unoccupied Molecular Orbital (LUMO). To bring light on the electronic state present near Fermi level with chemical stability of the considered system; one should have considered the

involvement of these orbitals situated on either side of the Fermi level those are mainly responsible for the variation in electronic states.

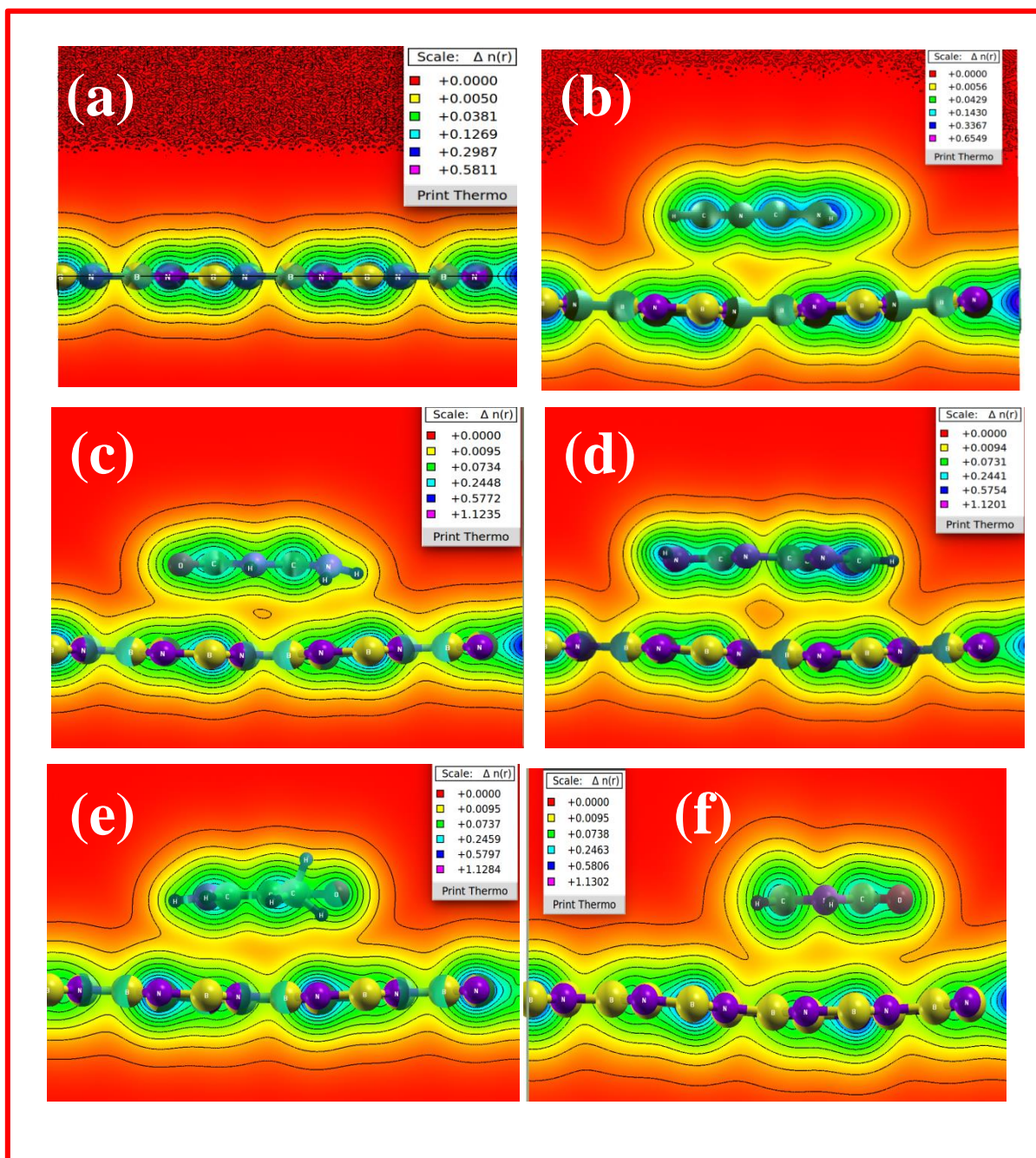
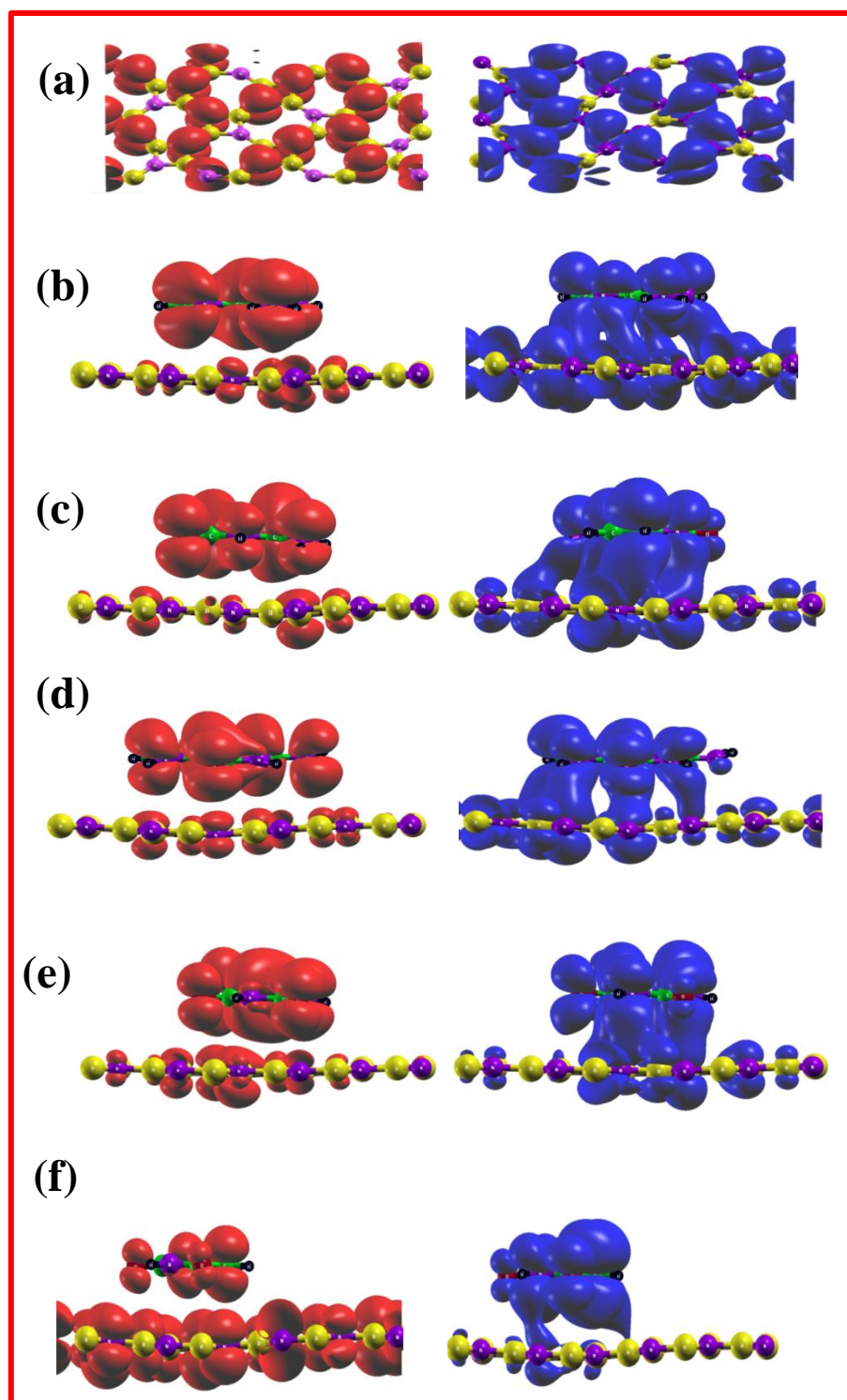


Figure 4.10: Charge density plot of (a) haeck-BN and haeck-BN adsorb by nucleobases (b) Adenine, (c) Cytosine, (d) Guanine, (e) Thymine, (f)Uracil.



*Figure 4.11: HOMO and LUMO of (a) haeck-BN and (b-f) nucleobase adsorbed haeck-BN system; (b) Adenine, (c) Cytosine, (d) Guanine, (e)*

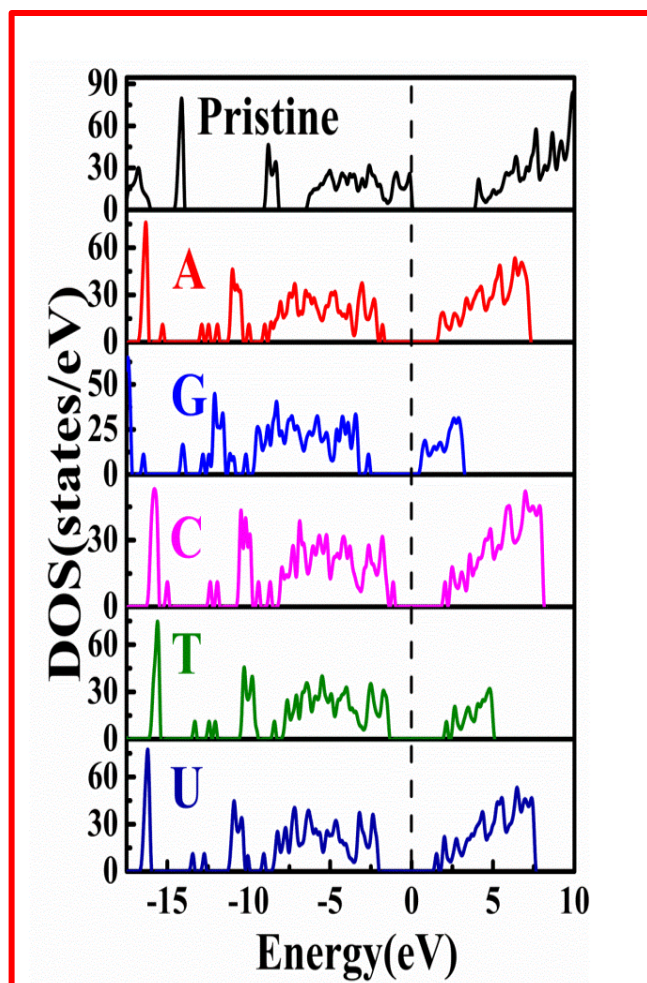
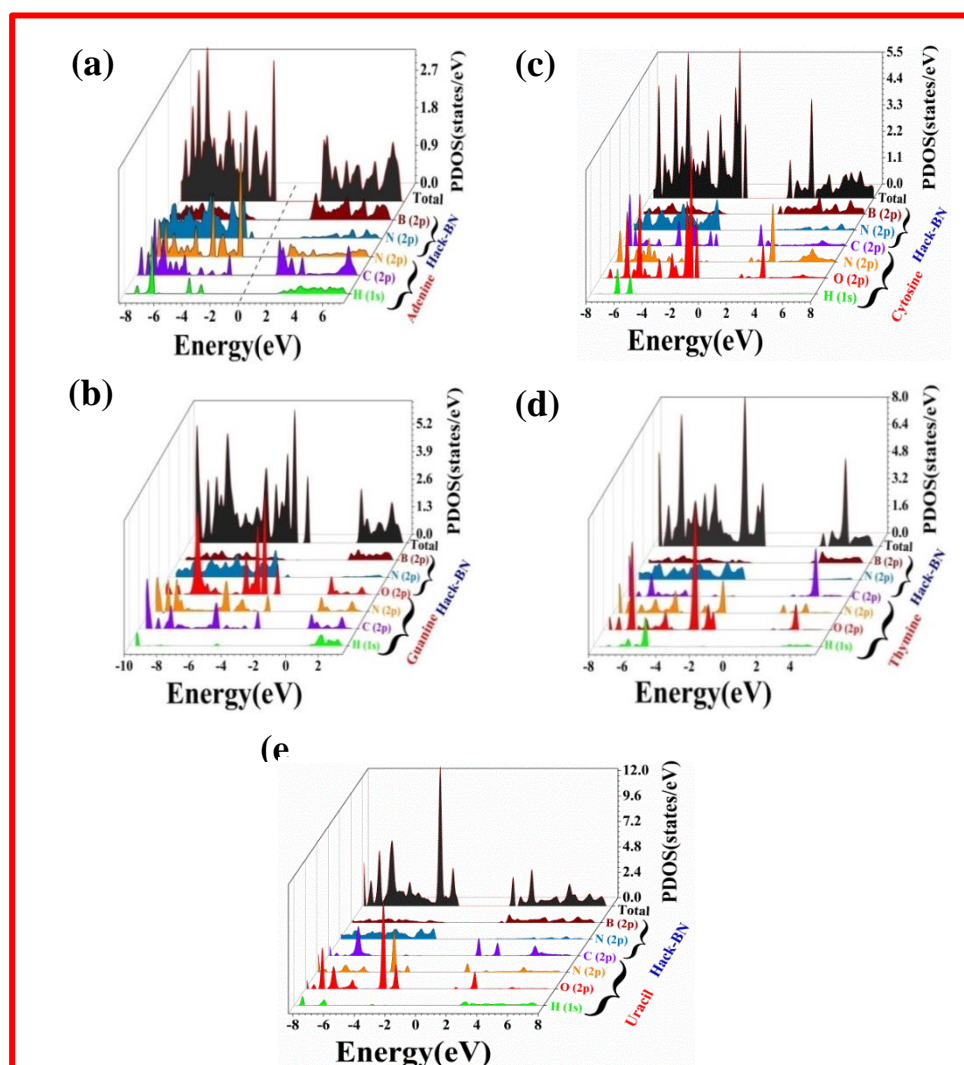


Figure 4.12 Electronic density of states (DOS) plot of pristine haeck-BN along with nucleobase adsorbed nucleobases.

Figure 4.11 systematically displays the HOMO and LUMO orbitals for considered systems in which we can see electronic cloud in both orbitals of pristine haeck-BN sheet which is distributed over the entire structure. Throughout the entire structure, electron cloud in HOMO is because of the N atom, while in LUMO it is due to B atom. The electronic states observed near the Fermi level is due to p orbital electrons present in B and N atoms which

can capture and lose electrons. After adsorption of nucleobases we see large differences in the HOMO and LUMO orbital electron clouds compared to haeck-BN (Fig. 4.11). In case of physisorbed nucleobases over haeck-BN sheet, LUMOs are more localized over N and O atoms with the clear indication of the electron transfer between N and O atoms of the nucleobases and for HOMO orbitals it is localized over B atoms.



**Figure 4.13** Partial density of states (PDOS) plot of nucleobases adsorbed haeck-BN system (a) Adenine, (b) Guanine, (c) Cytosine, (d) Thymine and (e) Uracil.

To analyze the electronic properties of the pristine as well as adsorbed molecules over haeck-BN sheet, we have calculated density of states (DOS) and partial density of states (PDOS), which are presented in Fig. 4.12 and Fig 4.13. For pristine haeck-BN, we observed that the valence band has major contribution at the Fermi level (See Fig. 4.12). The small peak appears at the -1.5 eV, -1.9 eV and -2.5 eV in the valence band region near Fermi level for the case of C, A and G, respectively after the interaction of haeck-BN sheet. Only C contributes to the conduction band, among the other three nucleobases. In case of U and T, electronic states arise at 1.7 eV and 2 eV in the conduction band region, respectively.

The DOS data clearly approves the alternation in the electronic properties of haeck-BN with major contribution in the lower valence band region between -10 eV to -15 eV, after the adsorption of nucleobases with the appearance of impurity. The creation of extra peak from the p-orbital electrons shows major contribution. The presence of NH<sub>2</sub> group in the molecule attributed to the appearance of some extra electronic states, which also modulates the band gap of pristine haeck-BN by the large amount (1.04 eV). Guanine is the strongest binding nucleobase with the largest adsorption energy over haeck-BN because of its structural and electronic properties; mainly due to the presence of oxygen atom which is a strong electron donor. The larger electronegativity of N and O atoms contribute to higher adsorption energy and extra pentagon with C, N and O attributed to the more polarization of molecule [81, 88]. To ascertain the electrical conductivity of materials the value of band gap is an important factor; because the energy required to remove an electron from the outer most shell to become a free movable charge carrier is equal to the bandgap.

The relation between  $E_g$  and electrical conductivity of a material can be given by the following relation [89]:

$$\sigma \propto e^{-E_g/2KT} \quad (4.3)$$

where  $K$  is the Boltzmanns constant and  $T$  is the temperature. From the above equation, one can say that the conductivity is inversely proportional to the bandgap, demonstrating that lower the value of bandgap  $E_g$  higher the electrical conductivity at a given temperature  $T$ . So, after the adsorption of nucleobases over the haeck-BN sheet, a significant decrement in the band gap increases in  $\sigma$  of the haeck-BN sheet. The trend in the increment in the  $\sigma$  is observed as:  $C > G > A > T > U$  after adsorption over haeck-BN. Accordingly, the strong interaction between the molecule and haeck-BN validates by the increment in the conductivity of the nanosheet. The adsorption of nucleobases originates an electrical signal due to the change in Fermi level of haeck-BN and therefore it could be a promising candidate for biosensor applications.

#### **4.3.4 Recovery Time and Work Function**

We have calculated the recovery time of haeck-BN to check its novelty as a carrier of nucleobases and its reusability. It is the so-called known parameter to elect the superiority of any sensor/detector/carrier with respect to such devices. Experimentally, the recovery time can be calculated by heating the substrate. Conversely, the computational approach to estimate the recovery time is based on transition theory. The required equation is expressed as [90]:

$$\tau = \nu^{-1} e^{-E_{ads}/KT} \quad (4.4)$$

Where  $\nu$  is the attempt frequency,  $K$  is the Boltzmann constant ( $\sim 8.318 \times 10^{-3}$  kJ/mol K) and  $T$  is the temperature. The value of attempt frequency is  $10^{12}$  s<sup>-1</sup> [21, 90-91] and we used temperature 298K, which have been incorporated to measure the recovery time for CNT from NO<sub>2</sub> molecule. By using this attempt frequency ultra-fast recovery time of 292 ms (millisecond), 130 ms, 120 ms, 160 ms and 0.6 ms is predicted for adsorbed G, A, C, T and U over haeck-BN, respectively.

The work function of pristine along with nucleobase-adsorbed haeck-BN sheet has been calculated to further check its sensing ability towards nucleobases. The work function  $\phi$  (eV) is the, value of energy needed to remove an electron from the upper-most filled level in the Fermi distribution of any material to a point in a field-free zone just outside the solid at an absolute temperature [64].

$$\phi(eV) = E_{vac} - E_F \quad (4.5)$$

where  $E_{vac}$  is the energy at vacuum level and  $E_F$  is Fermi level energy. By plotting the DOS from the lowest to higher energy level which gives the total number of electrons in a unit cell, we obtained the Fermi energy level.  $E_{vac}$  was determined by planar-average electrostatic potential energy along the direction of vacuum (z-direction) [64]. The work function ( $\phi$ ) plots are presented in Fig. 4.14. We determined two negative peaks on the curves of electrostatic potentials among them the strong peaks correspond to the haeck-BN nanosheet and weak peaks to the nucleobases. The work function is the difference in the electrostatic potentials between the Fermi and vacuum levels. After the adsorption of nucleobases over haeck-BN, a significant decrement in the work function ( $\phi$ ) is observed. The calculated 5.972 eV work

function of pristine haeck-BN is comparatively larger than that for other BN nanostructures [49, 92].

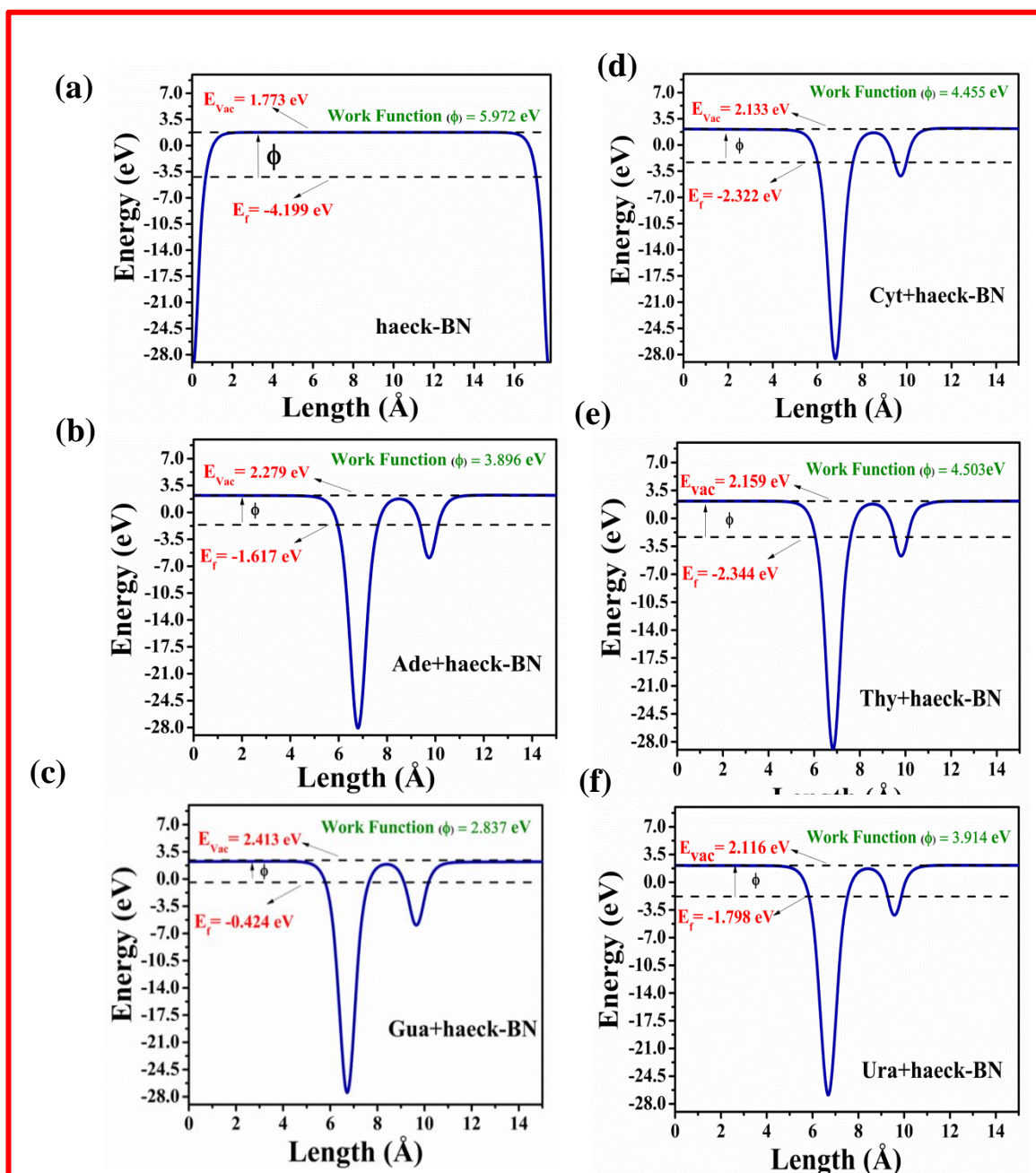


Figure 4.14: Work function plot of pristine and nucleobases adsorbed haeck-BN system (a) Pristine, (b) Adenine, (c) Guanine, (d) Cytosine, (e) Thymine and (f) Uracil.

The change in the work function ( $\phi$ ) has following trend: G (3.135 eV) > A (2.076 eV)  $\approx$  U (2.058 eV) > C (1.517 eV)  $\approx$  T (1.469 eV) (Table 4.4). The strong physical interaction between adsorbed nucleobases over haeck-BN sheet verifies by the alternation in work function. The large decrement in the work function attributed to the enhancement in the photocatalytic activity which indicates that smaller work function leads to higher catalytic activity.

The alternation in electronic properties after adsorption of nucleobases over haeck-BN proposes an easy detection of considered molecules. Lastly, considering our outcomes, it is found that nucleobase molecules are physisorbed over haeck-BN. Hence, this new boron nitride cousin is beneficial for the utilization in targeted delivery of the considered biomolecule and its reversibility is easy in case of physisorption compared to chemisorption. Our study points out that the haeck-BN is a good nominee for a biomolecule carrier, and it should be further explored for its utilization in a biomedical and photocatalytic applications.

#### **4.4 Conclusions**

In the present work, we studied the electronic properties of the newly proposed haeck-BN consisting square and octagonal rings, using the first principles calculations based on density functional theory. The phonon dispersion curves and phonon density of states confirm the kinetic stability of this haeckelite monolayer; with the absence of a single mode having imaginary frequency in the entire BZ. This new haeck-BN with direct band gap of 3.9 eV illustrates its semiconducting behavior with an advantage to be utilized for chemical as well as biosensor. To understand adsorption energetics of nucleobases over the haeck-BN surface the

adsorption energy of all considered systems are calculated with the incorporation of dispersion correction (DFT-D2). The comparison of adsorption mechanism of nucleobases with graphene, BNNT and haeck-BN was discussed in detail and among them haeck-BN is found with the superior performance. The adsorption trend of nucleobases over haeck-BN surface is:  $G > T > A \approx C > U$ . After adsorption, the changes in work function of nucleobases were found in order:  $G$  (3.135 eV)  $>$   $A$  (2.076 eV)  $\approx$   $U$  (2.058 eV)  $>$   $C$  (1.517 eV)  $>$   $T$  (1.469 eV) unlike the graphene and BNNT. It also approves the sensitivity of haeck-BN towards the nucleobases. We further calculated the recovery time to confirm the novelty of the haeck-BN as a biosensor. The calculated recovery time for  $G$  (292 ms),  $A$  (130 ms),  $C$  (120 ms),  $T$  (160 ms) and  $U$  (0.6 ms) is very low, which strengthens the possibility of haeck-BN for its reusability in application of biosensor. The significant change in electronic properties observed after the interaction between haeck-BN and nucleobases shows the possibility of for the utilization of haeck-BN for the detection of the considered nucleobases. Therefore, we may predict substitute to other h-BN and graphene systems intended for sensing applications for nucleobase as well as DNA sequencing. We believe that our outcomes will inspire experimentalist as well as theoretician to develop/predict new layered semiconducting materials.

## References

1. W. Krätschmer, L. D. Lamb, K. Fostiropoulos and D. R. Huffman, *Nature* **347**, 354 (1990).
2. D. S. Bethune, C. H. Kiang, M. S. de Vries, G. Gorman, R. Savoy, J. Vazquez and R. Beyers, *Nature* **363**, 605 (1993).

3. L. S. Ying, M. A. Bin Mohd Salleh, H. B. Mohamed Yusoff, S. B. Abdul Rashid and J. B. Abd. Razak, *J. Ind. Eng. Chem.* **17**, 367 (2011).
4. K. S. Novoselov, A. K. Geim, S. V. Morozov, D. Jiang, Y. Zhang, S. V. Dubonos, I. V. Grigorieva and A. A. Firsov, *Science* **306**, 666 (2004).
5. E. Pop, V. Varshney and A. K. Roy, *MRS Bull.* **37**, 1273 (2012).
6. X. Wang, L. Zhi and K. Müllen, *Nano Lett.* **8**, 323 (2008).
7. J. H. Chen, M. Ishigami, C. Jang, D. R. Hines, M. S. Fuhrer and E. D. Williams, *Adv. Mater.* **19**, 3623 (2007).
8. Y. Zhang, Y. W. Tan, H. L. Stormer and P. Kim, *Nature* **438**, 201 (2005).
9. S. V. Morozov, K. S. Novoselov, M. I. Katsnelson, F. Schedin, D. C. Elias, J. A. Jaszczak and A. K. Geim, *Phys. Rev. Lett.* **100**, 016602 (2008).
10. J. H. Chen, C. Jang, S. Adam, M. S. Fuhrer, E. D. Williams and M. Ishigami, *Nat. Phys.* **4**, 377 (2008).
11. S. S. Gregersen, S. R. Power and A. P. Jauho, *Phys. Rev. B* **95**, 121406 (2017).
12. F. Molitor, J. Güttinger, C. Stampfer, S. Dröscher, A. Jacobsen, T. Ihn and K. Ensslin, *J. Phys. Condens. Matt.* **23**, 243201 (2011).
13. J. Klinovaja and D. Loss, *Phys. Rev. B* **88**, 075404 (2013).
14. Y. Xu, Z. Gan and S. C. Zhang, *Phys. Rev. Lett.*, **112**, 226801 (2014).
15. Y. N. Xu and W. Y. Ching, *Phys. Rev. B* **44**, 7787 (1991).
16. W. Choi, N. Choudhary, G. H. Han, J. Park, D. Akinwande and Y. H. Lee, *Mater. Today* **20**, 116 (2017).
17. K. Takeda and K. Shiraishi, *Phys. Rev. B* **50**, 14916 (1994).
18. S. Cahangirov, M. Topsakal, E. Aktürk, H. Şahin and S. Ciraci, *Phys. Rev. Lett.* **102**, 236804 (2009).
19. H. Liu, A. T. Neal, Z. Zhu, Z. Luo, X. Xu, D. Tománek and P. D. Ye, *ACS Nano* **8**, 4033 (2014).
20. H. R. Sonia and P. K. Jha, *Solid State Commun.* **189**, 58 (2014).
21. K. Patel, B. Roondhe, S. D. Dabhi and P. K. Jha, *J. Hazard. Mater.* **351**, 337 (2018).

22. S. B. Pillai, S. Narayan, S. D. Dabhi and P. K. Jha, *AIP Conf. Proc.* **1731**, 090024 (2016).
23. S. B. Pillai, S. D. Dabhi, S. Narayan and P. K. Jha, *AIP Conf. Proc.* **1942**, 090022 (2018).
24. B. Feng, J. Zhang, Q. Zhong, W. Li, S. Li, H. Li, P. Cheng, S. Meng, L. Chen and K. Wu, *Nat. Chem.* **8**, 563 (2016).
25. A. Pakdel, C. Zhi, Y. Bando and D. Golberg, *Mater. Today* **15**, 256 (2012).
26. J. Yin, L. Jidong, Y. Hang, Y. Jin, G. Tai, L. Xuemei, Z. Zhang and W. Guo, *Small*, **12**, 2942 (2016).
27. A. Pakdel, Y. Bando and D. Golberg, *Chem. Soc. Rev.* **43**, 934 (2014).
28. C. R. Dean, A. F. Young, I. Meric, C. Lee, L. Wang, S. Sorgenfrei, K. Watanabe, T. Taniguchi, P. Kim, K. L. Shepard and J. Hone, *Nat. Nanotechnol.* **5**, 722 (2010).
29. P. Sutter, J. Lahiri, P. Zahl, B. Wang and E. Sutter, *Nano Lett.* **13**, 276 (2013).
30. X. Li, J. Yin, J. Zhou and W. Guo, *Nanotechnology* **25**, 105701 (2014).
31. G. H. Lee, Y. J. Yu, C. Lee, C. Dean, K. L. Shepard, P. Kim and J. Hone, *Appl. Phys. Lett.* **99**, 243114 (2011).
32. Q. Li, X. Zou, M. Liu, J. Sun, Y. Gao, Y. Qi, X. Zhou, B. I. Yakobson, Y. Zhang and Z. Liu, *Nano Lett.* **15**, 5804 (2015).
33. Y. Liu, X. Zou and B. I. Yakobson, *ACS Nano* **6**, 7053 (2012).
34. D. C. Camacho-Mojica and F. López-Urías, *Sci. Rep.* **5**, 1 (2015).
35. P. V. Gaikwad, P. K. Pujari, S. Chakroborty and A. Kshirsagar, *J. Phys. Condens. Matter* **29**, 335501 (2017).
36. X. Tu, S. Manohar, A. Jagota and M. Zheng, *Nature* **460**, 250 (2009).
37. D. Umadevi and G. N. Sastry, *J. Phys. Chem. Lett.* **2**, 1572 (2011).
38. C. Zhi, Y. Bando, W. Wang, C. Tang, H. Kuwahara and D. Golberg, *Chem. Asian J.* **2**, 1581 (2007).
39. G. Ciofani, V. Raffa, A. Menciasci and A. Cuschieri, *Biotechnol. Bioeng.* **101**, 850 (2008).

40. X. Chen, P. Wu, M. Rousseas, D. Okawa, Z. Gartner, A. Zettl and C. R. Bertozzi, *J. AM. Chem. Soc.* **131**, 890 (2009).
41. S. Liu, B. Lu, Q. Zhao, J. Li, T. Gao, Y. Chen, Y. Zhang, Z. Liu, Z. Fan, F. Yang, L. You and D. Yu, *Adv. Mater.* **25**, 4549 (2013).
42. L. Zhang and X. Wang, *Nanomaterials* **6**, 111 (2016).
43. B. Roondhe, S. D. Dabhi and P. K. Jha, *Appl. Surf. Sci.* **441**, 588 (2018).
44. Y. Zhao, Y. Xie, Z. Liu, X. Wang, Y. Chai and F. Yan, *Small* **10**, 4521 (2014).
45. Q. Lin, X. Zou, G. Zhou, R. Liu, J. Wu, J. Li and W. Duan, *Phys. Chem. Chem. Phys.* **13**, 12225 (2011).
46. K. Jin, L. Xie, Y. Tian and D. Liu, *J. Phys. Chem. C* **120**, 11204 (2016).
47. G. Ciofani, V. Raffa, J. Yu, Y. Chen, Y. Obata, S. Takeoka, A. Menciassi and A. Cuschieri, *Curr. Nanosci.* **5**, 33 (2009).
48. G. G. Genchi and G. Ciofani, *Nanomedicine* **10**, 3315 (2015).
49. S. D. Dabhi, B. Roondhe and P. K. Jha, *Phys. Chem. Chem. Phys.* **20**, 8943 (2018)
50. P. K. Jha and S. P. Sanyal, *Physica C* **261**, 259 (1996).
51. P. K. Jha, *Phys. Rev. B.* **72**, 214502 (2005).
52. P. K. Jha, S. D. Gupta and S. K. Gupta *AIP Advances* **2**, 022120 (2012).
53. M. Talati and P. K. Jha, *Phys. Rev. B.* **74**, 134406 (2006).
54. G. P. Srivastava The physics of phonons. CRC press (1990).
55. H.J. Maris (ed) Phonon scattering in condensed matter. Plenum Press, New York (1980).
56. G.K. Horton, A.A. Maradudin (Eds.), Dynamical Properties of Solids, vol. 3, North-Holland, Amsterdam (1980).
57. Z. Zhang, H. Huang, X. Yang and L. Zang, *J. Phys. Chem. Lett.* **2**, 2897 (2011).
58. T. Kar, H. F. Bettinger, S. Scheiner and A. K. Roy, *J. Phys. Chem. C* **112**, 20070 (2008).
59. P. Giannozzi, et al. *J. Phys. Condens. Matter* **21**, 395502 (2009).
60. J. D. Head and M. C. Zerner, *Chem. Phys. Lett.* **122**, 264 (1985).
61. J. P. Perdew, K. Burke and M. Ernzerhof, *Phys. Rev. Lett.* **77**, 3865 (1996).

62. H. J. Monkhorst and J. D. Pack, *Phys. Rev. B.* **13**, 5188 (1976).
63. S. Baroni, S. De Gironcoli, A. Dal Corso and P. Giannozzi, *Rev. Mod. Phys.* **73**, 515 (2001).
64. C. Kittel, *Introduction to Solid State Physics*, John Wiley & Sons, Inc, United States, 2010.
65. S. Grimme, *Semiempirical J. Comput. Chem.* **27**, 1787 (2006).
66. M. Topsakal, E. Aktürk and S. Ciraci, *Phys. Rev. B.* **79**, 115442 (2009).
67. E. Kroumova, M. L. Aroyo, J. M. Perez-Mato, A. Kirov, C. Capillas, S. Ivantchev and H. Wondratschek, *Phase Transitions* **76**, 155 (2003).
68. S. Barua, H. S. Dutta, S. Gogoi, R. Devi and R. Khan, *ACS Appl. Nano Mater.* **1**, 2 (2018).
69. S. D. Gupta, S. K. Gupta, P. K. Jha and N. N. Ovsiuk, *J. Raman Spectro.* **44**, 926 (2013).
70. S. D. Gupta and P. K. Jha, *Earth Planet. Sci. Lett.* **401**, 31 (2014).
71. P. Anees, M. C. Valsakumar and B. K. Panigrahi, *Phys. Chem. Chem. Phys.* **18**, 2672 (2016).
72. P. K. Jha and H. R. Soni, *J. Appl. Phys.* **115**, 023509 (2014).
73. I. Lifshitz, *Zh. Eksp. Teor. Fiz* **22**, 475 (1952).
74. M. S. Dresselhaus, *Physical Properties of Carbon Nanotubes*, Imperial College Press, London, 2005.
75. C. Marchbanks and Z. Wu, *J. Appl. Phys.* **117**, 084305 (2015).
76. J.-Y. Lin, P. L. Ho, H. L. Huang, P. H. Lin, Y.-L. Zhang, R.-C. Yu, C.-Q. Jin and H. D. Yang, *Phys. Rev. B* **67**, 052501 (2003).
77. W. Lu, X. Liu, S. Liu, W. Cao, Y. Zhang and P. Yang, *Sci. Rep.*, **7**, 1 (2017).
78. E. C. Anota, Y. Tlapale, M. S. Villanueva and J. A. R. Márquez, *J Mol. Model.* **21**, 215 (2015).
79. S. Grimme, J. Antony, S. Ehrlich and H. Krieg, *J. Chem. Phys.* **132**, 154104 (2010).
80. J. B. A. Davis, F. Baletto and R. L. Johnston, *J. Phys. Chem. A* **119**, 9703 (2015).
81. N. Ding, X. Chen, C.-M. L. Wu and H. Li, *Phys. Chem. Chem. Phys.* **15**, 10767 (2013).

82. S. Gowtham, R. H. Scheicher, R. Ahuja, R. Pandey and S. P. Karna, *Phys. Rev. B.* **76** , 033401 (2007).
83. H. H. Gürel and B. Salmankurt, *Mater. Res. Express* **4**, 065401 (2017).
84. P. Han, K. Akagi, F. Federici Canova, H. Mutoh, S. Shiraki, K. Iwaya, P. S. Weiss, N. Asao and T. Hitosugi, *ACS Nano* **8**, 9181 (2014).
85. K. Müller-Dethlefs and P. Hobza, *Chem. Rev.* **100**, 143 (2000).
86. S. Mukhopadhyay, S. Gowtham and R. H. Scheicher, *Nanotechnology* **21**, 165703 (2010).
87. Z. Gulácsi, *Eur. Phys. J. B* **87**, 143 (2014).
88. F. Erkoç and Sakir Erkoç, *J. Mol. Struct. THEOCHEM*, **589**, 405 (2002).
89. S. S. Li, *Semiconductor Physical Electronics*, Springer Science, United States, 1997.
90. Z. Rostami, M. Pashangpour and R. Moradi, *J. Mol. Graph. Model.* **72**, 129 (2017).
91. S. Peng, K. Cho, P. Qi and H. Dai, *Chem. Phys. Lett.* **387**, 271 (2004).
92. F. Schulz, R. Drost, S. K. Hämäläinen, T. Demonchaux, A. P. Seitsonen and P. Liljeroth, *Phys. Rev. B* **89**, 235429 (2014).